communications physics

A Nature Portfolio journal

Article

https://doi.org/10.1038/s42005-025-02094-1

Controlling colloidal flow through a microfluidic Y-junction

Check for updates

Alexander P. Antonov [1,5], Matthew Terkel[2,3,5], Fabian Jan Schwarzendahl[1], Carolina Rodríguez-Gallo [2,3,4], Pietro Tierno [2,3] & Hartmut Löwen[1]

Microscopic particles flowing through narrow channels may accumulate near bifurcation points provoking flow reduction, clogging and ultimately chip breakage in a microfluidic device. Here we show that the full flow behavior of colloidal particles through a microfluidic Y-junction can be controlled by tuning the pair interactions and the degree of confinement. By combining experiments with numerical simulations, we investigate the dynamic states emerging when magnetizable colloids flow through a symmetric Y-junction such that a single particle can pass through both gates with the same probability. We show that clogging, induced by the inevitable presence of a stagnation point, can be avoided by repulsive interactions. Moreover we tune the pair interactions to steer branching into the two channels: attractive particles are flowing through the same gate, while repulsive colloids alternate between the two gates. Even details of the particle assembly such as buckling at the exit gate are tunable by the interactions and the channel geometry.

Understanding the flow of particulate matter through narrow channels is of paramount importance for many applications, both in the natural[1–3] and in the synthetic[4–6] world. Examples can be found on different length scales ranging from molecular over mesoscopic to macroscopic sizes. Permeation of molecules through nanopores and zeolites[7] constitutes a prime example on the molecular scale while the flow of red blood cells in the vascular system[8,9] and synthetic colloids near constrictions[10–12] are topics that fall within the colloidal regime. On the macroscopic scale, the escape of pedestrians or animals through narrow gates[13,14], airplane boarding[15,16], crowded bikers in narrow streets[17] and the flow of grains through silos[18–21] provide other situations known from everyday life for confined flow problems.

The transport of particles near a branching point, such as a Y-junction, which splits the flow into two streams of fluids is of particular importance. Indeed, any nontrivial flow network is made of branching points which motivates to study a single Y-junction as a basic building block in the first place. Key examples are biological flow networks such as the blood circulation system[22] or synthetic ones[23,24]. Moreover, Y-junctions occur on various length scales, from nano-sized channel junctions, such as those in carbon nanotubes[25], to micron-sized artificial Y-junctions (or in extreme cases, T-junctions) in microfluidic circuits[26–28] or active agents[29]. At the microscale, confined particles forced to pass through a bifurcation path may accumulate near a stagnation point and induce clogging, via formation of bridges and arches that block the flow[19]. This effect is responsible for the failure of different technological systems, spanning from microfluidic chips[30,31], to silos[13], and granular hoppers[14,32]. Thus, understanding and controlling the emergence of clogging within simple bifurcation points such as a Y-junction is especially important. Moreover, within microfluidic chips, clogging has been explored for channels usually much wider than the particle diameter[30,33,34], but not for extreme narrow ones where flow blockage can be induced by the sudden channel widening near a junction.

Despite the fundamental significance of branching points, most of the research to date has focused either on particle transport through wide channels[35–42] or on tuning the interparticle interactions during flow[43–45], which is an important mechanism for controlling the flow itself. Theoretical works have highlighted the importance of branching points for particle separations at a T-junction[28] or their relationship with biological flow networks as blood transportation vasculature[46]. Indeed Y-junctions are more commonly used for merging rather than splitting, either to produce Janus particles[47,48] or in flow cytometry[49].

Here, we investigate the flow of strongly confined and interacting colloidal particles through a Y-junction. The Y-junction is symmetric such that a single particle can pass through both gates with the same probability. We use an external field to tune the pair interaction between magnetizable paramagnetic colloids. Our finding is that the flow behavior can be entirely tuned by the particle interactions and the geometry of the microfluidic channel. There is flow control on all levels: the basic switch from clogging to unclogging, the partition of particles into the two different gates and even

[1]Institut für Theoretische Physik II: Weiche Materie, Heinrich-Heine-Universität Düsseldorf, Düsseldorf, Germany. [2]Departament de Física de la Matèria Condensada, Universitat de Barcelona, Barcelona, 08028, Spain. [3]Universitat de Barcelona Institute of Complex Systems, Barcelona, 08028, Spain. [4]Institute for Bioengineering of Catalonia, Barcelona, 08028, Spain. [5]These authors contributed equally: Alexander P. Antonov, Matthew Terkel. e-mail: ptierno@ub.edu

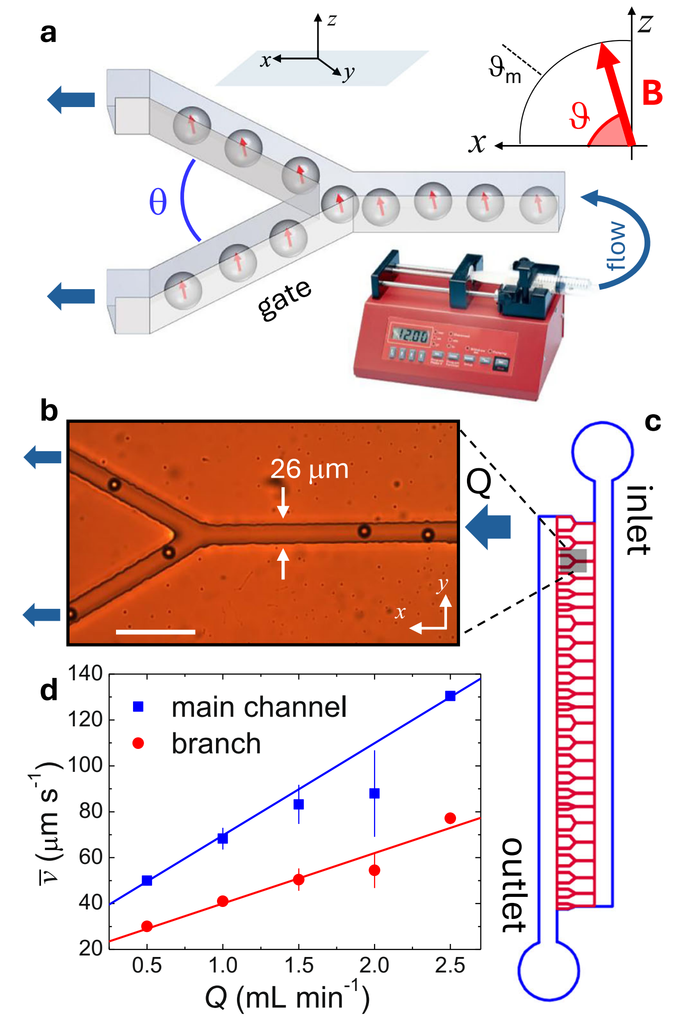

Fig. 1 | The microfluidic Y-junction. a Schematic of the experimental system: a syringe pump forces a collection of paramagnetic colloidal particles to flow through a Y-junction connecting two branches at an angle $\theta = 55°$. The pair interactions between the particles are tuned by an external magnetic field $\boldsymbol{B}$ applied at an inclination angle $\vartheta \in [0, 90]°$, being $\vartheta_m = 54.7°$ the "magic angle" delineating attractive ($\vartheta < \vartheta_m$) from repulsive ($\vartheta > \vartheta_m$) forces. **b** Optical microscope image of one channel with flowing particles, scale bar is 100 µm. See also Supplementary Movie 1. **c** Schematic of the microfluidic chip. **d** Average particle velocity $\bar{v}$ versus flow rate Q within the main channel (squares) and within the branches (disks). The experimental data are averaged over different independent measurements, and the error bars are obtained from the standard error.

details in the buckled structure formed by the flowing colloids. In particular, we find a tunable nonequilibrium branching transition between two distinct flowing regimes: a state where all particles pass through the same gate and another one where subsequent particles consecutively choose a different gate.

Results

The microfluidic Y-junction system

Figure 1a, c show two schematics of the experimental system (a) and of the microfluidic chip (c). The latter was fabricated in polydimethylsiloxane (PDMS) combining UV-irradiation and soft lithography, see more technical details in the Method Section. The whole chip is characterized by a series of bifurcations in form of Y-junctions connecting rectangular microfluidic channels with a constant lateral width of $d = 26.3 \pm 0.2$ µm and elevation $h \sim 100$ µm, Fig. 1b. Through these channels we disperse a water solution of paramagnetic polystyrene particles of diameter $\sigma = 18.8 \pm 0.4$ µm and magnetic volume susceptibility $\chi = 0.014$. Once in the channel, the particles sediment near the bottom plate (gravity pointing along the z-direction) due to density mismatch, and display negligible thermal fluctuations due to their relative large size. We use a syringe pump to apply a constant flow rate $Q \in [0.1, 2.5]\,\mu\mathrm{L\,min}^{-1}$ which induces an average speed $\bar{v} \sim Q/A$ to each particle, being $A = d \times h$ the cross-sectional area, see Supplementary Movie 1. Figure 1d shows the average velocity $\bar{v}$ measured for single particles both in the main channel and in one of the two branches. Since all channels have approximately the same cross-sectional area, by flow conservation the velocity reduces by half when the particles enter the branches after the Y-junction. In most of the experiments we use a small input flow such that $\bar{v} \sim 5\,\mu\mathrm{m\,s}^{-1}$ which correspond to a large Péclet number, $Pe = \bar{v}\sigma/(2D_0) \simeq 5000$ where the diffusion coefficient is negligibly small, $D_0 \sim 0.01$ µm^2 s^{-1}. During transport the particles are strongly confined between the microfluidic walls and the bottom glass substrate, and $\sigma = 0.71d$ so that they cannot overpass each other realizing a driven single file[50–54]. This situation is different than previous works on flow of concentrated colloidal suspension[55–58] where particle overtaking was possible and velocity oscillations were observed for intermediate confinement.

Particle transport and clogging

We now consider the collective transport of many particles. The sequence of images in Fig. 2a shows the typical situation encountered when an initially aligned chain of paramagnetic colloids is driven across the most symmetric Y-junction, $\theta = 90°$, and in absence of any applied field. The particles behave as hard spheres, and close to the bifurcation point rather than choosing one of the two exit gates, they form a permanent clog reducing their velocity to zero and impeding any further transport. Near this point the channel becomes wide enough that two or three particles can pass together forming an arch, which would completely block the transport of the remaining particles, see Supplementary Movie 2. To understand the physical origin of this behavior, a close inspection of the Y-junction shape reveals a small but non negligible flat wedge present at the bifurcation point, Fig. 2b. This imperfection results from the high aspect ratio of our channel, which inevitably induces a loss of resolution during the transfer process from the original mask, to a resin (SU-8 2100) and the PDMS chip. Indeed the presence of a flat wedge for high aspect ratio microfluidc channels is well know in the field of microfluidic fabrication[59] and this imperfection will be present in all chips investigated. Close to this flat wedge the fluid flow velocity $\mathbf{u} = (u_x, u_y)$ vanishes since it generates a stagnation point. We confirm this hypothesis by solving the incompressible Navier-Stokes equations in two dimensions for this specific geometry with the flat edge:

$$\frac{\partial \mathbf{u}}{\partial t} + (\mathbf{u} \cdot \nabla)\mathbf{u} = -\frac{1}{\rho_f}\nabla p + \nu \nabla^2 \mathbf{u} \tag{1a}$$

$$\nabla \cdot \mathbf{u} = 0, \tag{1b}$$

where t is the time, p is the pressure, ρ_f is the density of the fluid, and ν is the kinematic viscosity. The corresponding flow profile shown in Fig. 2c effectively displays a zero velocity region corresponding to the flatness of the bifurcation point. The presence of this "stagnation point" can be considered as a physical obstacle that can induce clogging. Thus, in this work we investigate the way our driven particles can overpass it. More technical details on the boundary conditions are given in the Method Section.

Unclogging via tunable interactions

To unclog the system, we repeat the experiments and control the pair interactions between the particles using an external magnetic field $\boldsymbol{B} \equiv B_x\hat{\boldsymbol{x}} + B_z\hat{\boldsymbol{z}}$ applied along the $(\hat{\boldsymbol{x}}, \hat{\boldsymbol{z}})$ plane, Fig. 1a. Here we fix $B = 8$ mT and vary only the inclination angle ϑ, defined as $\vartheta = \tan^{-1}(B_z/B_x)$. Under the applied field each particle acquires an induced dipole moment $\boldsymbol{m} = \pi\sigma^3\chi\boldsymbol{B}/(6\mu_0)$ pointing along the field direction, μ_0 being the permeability of the medium (water). Thus, a pair of particles (i, j) at relative position $r_{ij} = |\boldsymbol{r}_i - \boldsymbol{r}_j|$

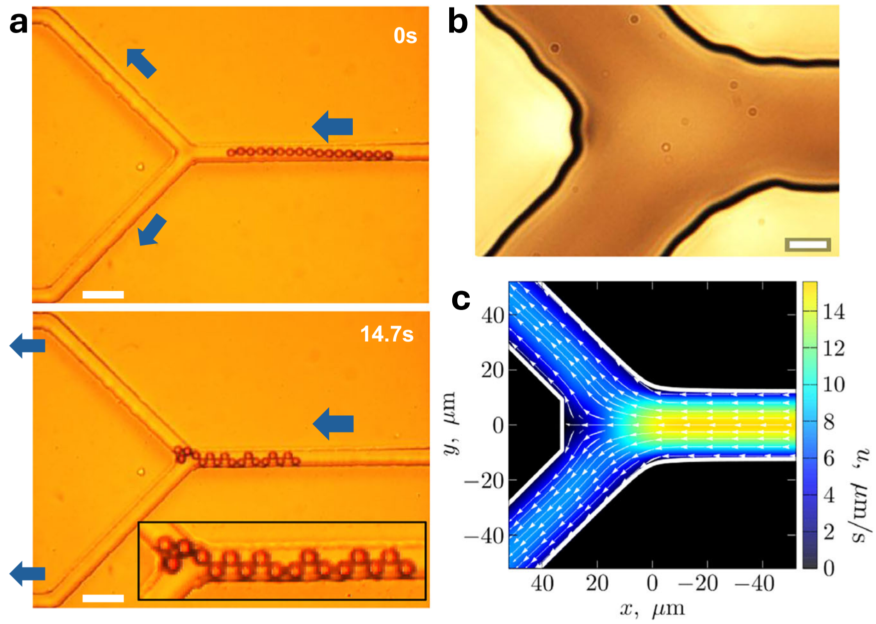

Fig. 2 | Clogging and flat tip at the Y-junction. **a** Clogging of a chain of paramagnetic colloids within a Y-junction with $\theta = 90°$ driven at an input flow rate $Q = 0.2\,\mu\text{L min}^{-1}$. Inset shows a small enlargement of the clogged state, scale bar is 100 μm. The corresponding video is Supplementary Movie 2. **b** Enlargement of the Y-junction section showing the absence of a sharp tip at the bifurcation point. Scale bar is 10 μm. **c** Flow profile obtained by solving Eqs. (1) within a Y-junction with the lithographic imperfection.

experiences magnetic dipolar interactions,

$$U_{dd}(r_{ij}) = -\frac{\mu_0 m^2}{2\pi r_{ij}^3} P_2(\cos\vartheta) \tag{2}$$

with $P_2(\cos\vartheta) = (3\cos^2\vartheta - 1)/2$ being the second order Legendre polynomial, see Chapter 5 in ref. 60 for a derivation. For an in-plane field ($\vartheta = 0°$) $P_2(\cos\vartheta) = 1$ dipolar interactions are attractive, and the particles within the microfluidic channel condense into a linear chain. In contrast, for a perpendicular field ($\vartheta = 90°$), $P_2(\cos\vartheta) = -1/2$, and the dipolar potential becomes $U_{dd} = \mu_0 m^2/(4\pi r_{ij}^3)$. This potential is isotropic and repulsive since the induced moments are perpendicular to their separation distance r_{ij}. Thus, the inclination angle ϑ induces the transition between two different flowing states. For strong attractive interactions, all particles flow through the same gate after crossing the bifurcation point, left column Fig. 3a. For strong repulsion, the driven particles choose alternating gates, right column in Fig. 3a. In both cases, the flowing colloids are not captured by the stagnation point and system clogging is prevented. The transition between both dynamic regimes can be characterized in terms of an effective magnetization $M \equiv |N_\uparrow - N_\downarrow|/N$ being $N_\uparrow$ ($N_\downarrow$) the number of particles that enters the upper (lower) branch, Fig. 3b. Thus, $M = 1$ corresponds to the absence of splitting, which is observed in the channel before the junction and for strong, attractive interactions, $\vartheta < 45°$. Here the particles minimize their distance such that the normalized particle density, $\rho = N\sigma/L \sim 1$ where L is the length of the chain (distance between the leading edge of the first particle and the trailing edge of the last particle) prior to inducing the fluid flow. In contrast, for $\vartheta > 60°$, the particles display initially a small transverse buckling just prior to reaching the Y-junction entrance with the density $\rho < 1$, which decreases initially the value of ρ as shown in the state diagram in Fig. 3b. Close to the magic angle, repulsion and attraction are balanced but the particles are still magnetized due to the presence of the applied field. Thus, we did not recover the clogging since second-order anisotropies, such as quadrupolar and hexapole-dipole interactions[61] are not zero, and may still affect the particle flow. We note that the different error bars in Fig. 3b for cone angles $\vartheta \in [60, 80]°$ are due to the fact that, for intermediate repulsion, the paramagnetic colloids may not be all aligned close to the side walls of the channel in the zigzag pattern. This could produce a slightly different relative velocity, with a variation in the measured density. At the junction, the particles separate following the two gates in an alternating way, thus reducing the value of M which vanishes as all particles exit the central channel. We note that by definition M is not exactly zero for branching chains with an odd number of particles. The transition is smooth and crosses the magic angle where magnetic interactions are minimized. At the channel entrance, when the field is applied, attractive particles form straight chains, while repulsive particles arrange into a zig-zag pattern, Fig. 2a. In a stable laminar flow regime, particles tend to follow the branching channel of the wall closer to their initial location. As a result, repulsive particles are more likely to exhibit branching behavior, as shown in the right column of Fig. 3a. Thus, the branching mechanism can be summarized as follows: attractive interactions cause particles to chain along the same streamline, inducing their motion along the same channel. In contrast, repulsive interactions drive the particles initially apart, thus directing them into different channels, see also Supplementary Movie 3. We also note that the channel width plays a crucial role in determining the flow properties. For example, the specific clogging configuration shown in Fig. 2a with particles arranged in triangular form would not be possible for smaller channel diameters. The sensitivity of the flow properties on the channel width is thus further analyzed using numerical simulations.

Numerical simulations: confinement and buckling

We complement the experimental data with numerical simulations, as shown in Fig. 3b. In the simulations, we consider a set of $i = 1, \ldots, N$ particles, at position $\mathbf{r}_i$, which obey the overdamped equations of motion:

$$\frac{\mathrm{d}\mathbf{r}_i}{\mathrm{d}t} = \mathbf{u}(\mathbf{r}_i) - \frac{1}{\gamma}\nabla\left[\sum_{j\neq i} U_\mathrm{p}(|\mathbf{r}_i - \mathbf{r}_j|) + U_\mathrm{w}(\mathbf{r}_i)\right]. \tag{3}$$

Here $\boldsymbol{u}$ is the flow field calculated from Eqs. (1), γ is the Stokes friction coefficient, U_p and U_w describe respectively the interaction between the particles and with the channel wall. The former are given via a combination of a Weeks-Chandler-Anderson (WCA) repulsive potential, U_WCA, and the dipole-dipole interaction, $U_\mathrm{p}(\mathbf{r}_{ij}) = U_\mathrm{WCA}(\mathbf{r}_{ij}) + U_{dd}(\mathbf{r}_{ij})$. More technical details are given in the Method Section.

Apart from confirming the experimental data, the simulations allow us to set the initial particle position in the chain and to tune the particle size within the channel, which are two parameters difficult to control in experiments. We observe that the lateral confinement strongly influences the dynamic states and the chain deformations via buckling in one of the two branches. In the sequence of images in Fig. 4a, we show that the branching transition $M = 1 \to M = 0$ can be also induced by increasing the size ratio σ/d, where $M = 1$ for $\sigma < 0.73d$ and $M = 0$ for $\sigma > 0.92d$ for all field inclination

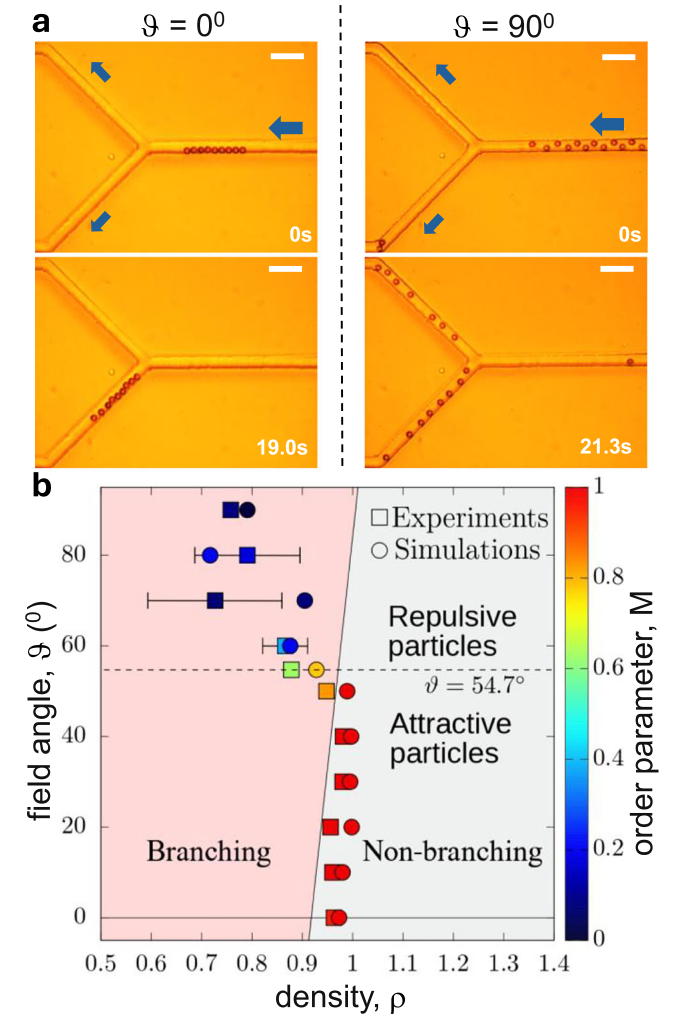

Fig. 3 | Field induced branching behavior at the Y-junction. a Sequence of images showing a train of paramagnetic colloidal particles flowing through a Y-junction with $\theta = 90°$. Left (right) column illustrates the case of attractive (repulsive) interactions induced by an in-plane field $\vartheta = 0°$ (out of plane field, $\vartheta = 90°$, resp.). Scale bar for all images is 100 μm, see Supplementary Movie 3. **b** Order parameter M in the (ρ, ϑ) plane, with $\rho = N\sigma/L$ denoting the normalized particle density. Scattered squares (disks) are experimental (simulation) data. The dashed line indicates $\vartheta = 54.7°$. The straight line that separate branching and non-branching behavior is a guide to the eye. The experimental data are averaged over different independent measurements, and the error bars are obtained from the standard error.

angles ϑ. Effectively, the full state diagram in the $(\vartheta, \sigma/d)$ plane in Fig. 4b shows that this transition becomes independent from the pair interactions. For strong confinement, the chain of particles enters the Y-junction reducing its speed at contact with the flat edge (stagnation point) and subsequently the pressure from the nearest incoming particle induces coiling and subsequent splitting between the two branches. In this situation excluded volume interactions dominate the final dynamic regime. In contrast, smaller particles display a stronger lateral mobility and are able to overcome the stagnation point when initially driven along a streamline of the flow (Supplementary Movie 4). Note that, in Fig. 3b the initial particle position was the same as the experimental ones. In contrast, in Fig. 4b we impose the straight-line initial condition for all field angles to eliminate the effect of particle initialization on the branch selection.

Note that, in Fig. 3b the initial particle position was the same as the experimental ones. In contrast, in Fig. 4b we impose the straight-line initial condition for all field angles to eliminate the effect of particle initialization on the branch selection. As shown in Fig. 4c, for high flow rate and at parity of magnetic field parameters, the transition is favored due to increase of the momentum that carry the driven particles which allow them to easily pass the stagnation point. This behavior is confirmed in experiments, as shown by Supplementary Movie 5 where, at parity of applied field ($\vartheta = 0°$, $B = 8$mT), the order parameter decreases when increasing flow rate, $M = 1$ for $Q = 0.1\,\mu\mathrm{L\,min}^{-1}$ and $M = 0.75$ for $Q = 0.5\,\mu\mathrm{L\,min}^{-1}$. Overall, the intricate interplay between stagnation point effects and particle confinement leads to a non-monotonic dependence of the order parameter M on the particle diameter, as shown in Fig. 4b, c.

Finally an intriguing consequence of the effect of confinement is the emergence of a buckled state within the exit gate, as shown in the enlarged insets in Fig. 4a. This effect can be quantified by measuring the chain roughening at the exit gate defined as, $W^2 = N^{-1}\sum_{i=1}^{N}\langle h_i^2\rangle$, being h_i, $i = 1...N$ the displacement of the particle i from the center of the corresponding branching channel after the bifurcation point, such that for $h_i = 0$ the particle is exactly at the channel center. In Fig. 4d we show the roughness extracted from the particle positions by varying the size ratio σ/d and normalized such that its maximum observed value is set to 1. The corresponding diagram in the $(\sigma/d, \vartheta)$ plane shows a re-entrant behavior where buckling is observed only for intermediate particle sizes, $\sigma/d \in [0.71, 0.89]$. For small size, the particles do not enter the stagnation point when initially located near the walls in the main channel. Therefore, they follow the streamline of the laminar flow and do not form any buckled configuration. By increasing the diameter, the particles are more likely to enter the stagnation point. However, for $\sigma/d > 0.89$ the stricter confinement impedes any chain deformation. Thus, the channel size can be used to control the colloidal assembly process at the exit gate, allowing to produce both straight or buckled structures that continuously flow along the channel.

Discussion

We have shown that tuning the pair interactions between strongly confined flowing particles can be used to avoid clogging near bifurcation points and to control the flow splitting into the two exit gates. The observed non-equilibrium branching transition at the Y-junction can be induced both by the applied field or by the confinement itself. The latter can also be used to control the colloidal assembly process by inducing buckling, which become absent for the extreme cases of large or small size ratio.

The physical situation explored with our flowing colloidal chain is also close to many biological systems. For example red-blood cells within narrow capillaries are forced to proceed through narrow pores in the form of a single file[62]. In addition, recent works have investigated the diffusive[23] and transport[63] properties of deformable particles, as blood cell, through an extended honeycomb network of Y-junctions. While blood cells can deform to easily overcome bifurcation points, other biological entities such as bacteria are relatively stiffer[64,65], presenting soft interactions similar to our dipolar colloids. Our work used paramagnetic colloids as model system to investigate the emergence of the branching transition when tuning the pair interactions from repulsive to attractive. However, repulsive or attractive interactions between non-magnetic particles can also be tuned. For example, highly charged particles in low polar solvents may display long Debye screening length[66] and induce repulsive forces which can be tuned by varying the amount of dispersed salt[67]. On the other hand, attractive forces can be induced by dispersing in the medium a non adsorbing polymer[68]. In the last case, one can tune the strength of the attraction by varying the polymer concentration[69]. Additionally, our findings apply not only to systems where the interactions can be tuned, but also to those characterized by fixed repulsive or attractive interactions.

Finally, a potential future direction could be to disperse the particles within a viscoelastic medium[70] to further mimic biological environments. This may lead to memory effects and further enrich the transition diagram unveiled by our work.

Methods

Experimental details

The microfluidic chip shown in Fig. 1b is designed and fabricated using microfabrication protocols. In particular, a 5-inch silicon (Si) wafer is first

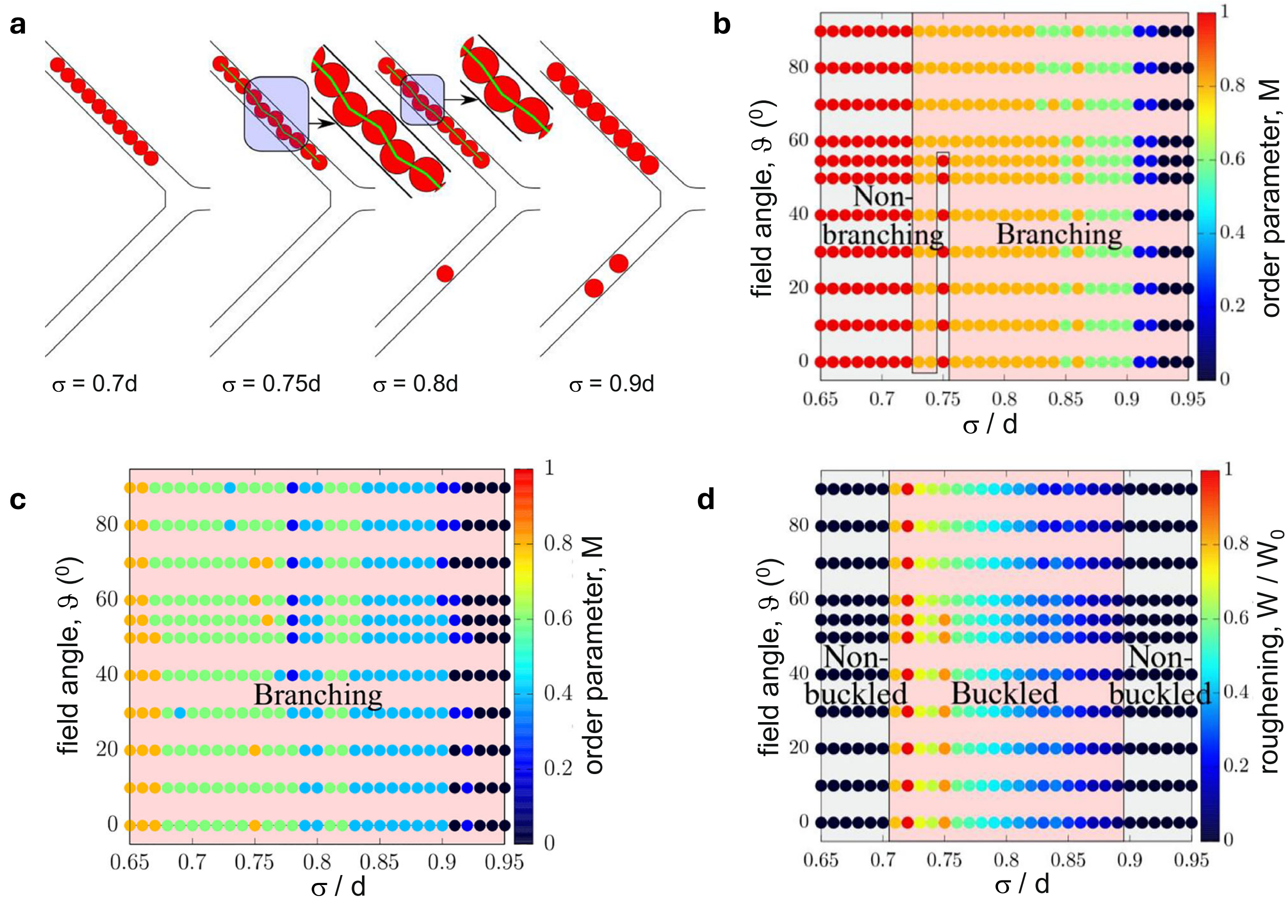

Fig. 4 | Buckling during branching at the Y-junction. **a** Simulation snapshots ($\vartheta = 0°$) showing the transition between the buckled and non-buckled states and the splitting induced by varying the normalized particle size σ/d. Buckling is highlighted in the top insets for $\sigma = 0.75d$ and $\sigma = 0.8d$, see Supplementary Movie 4. **b** Order parameter M in the (σ/d, ϑ) plane from numerical simulations. **c** Branching transitions induced by a flow rate $Q = 0.4\,\mu\text{L min}^{-1}$ showing that, at parity of field parameters, the branching behavior is enhanced by doubling the flow rate. **d** Normalized roughening W/W_0 of the colloidal chain in the (σ/d, ϑ) plane showing the buckled regions at the exit gate.

prepared by spin coating (Laurell Tech, WS-650) a thin layer (~100 μm in height) of SU-8 2100 epoxy-based photoresist. A mask aligner (SÜSS Microtec, Model MJB4) is used to transfer a flexible film photomasks to the photoresist-coated Si wafer. The latter is exposed to UV light at an intensity of 240 mJ cm^{-2} for 18.46 s. A post exposure bake (JP Selecta Plactronic hotplate) is performed on the wafer for 5 min at 65 °C followed by 10 min at 95 °C. After that the wafer is developed for 10 min being submerged in propylene glycol monomethyl ether acetate, rinsed with isopropanol and dried with nitrogen gas. Finally, the wafer is hard baked for 30 min at 95 °C followed by 10 min at 65 °C. A silanization process is carried out by placing the wafer next to a drop of Silane (SiH_4) inside of a vacuum chamber and left for at least an hour. The wafer is then placed in a petri dish along with a 0.5 cm thick layer of polydimethylsiloxane (PDMS, SYLGARD 184 Silicone Elastomer Kit, Sigma Aldrich), and left to cure for 4 h at 65 °C (Thermo Scientific, Heratherm oven). A plasma cleaner (Harrick, PCD-002-CE) is used to prepare the PDMS chips and glass cover slip (Menzel-Gläser) surfaces for a secure bonding.

The colloidal suspension is prepared by diluting 200 μL of the magnetic polystyrene particle solution (diameter $\sigma = 18.82 \pm 0.40$ μm, 5% w/v, iron oxide >15 wt%, microParticles GmbH) with 13 mL of ultrapure water (Milli-Q) and 0.5 g of sodium dodecyl sulfate (SDS, Sigma Aldrich). For each microfluidic experiment the chip is first flooded with the colloidal suspension to remove all air bubbles from the device. Then, a permanent magnet is used to attract the magnetic particles into the straight channel of the Y-junction forming a chain of particles due to attractive magnetic dipolar interactions. The channels in the Y-junction have a width of $d = 26.3 \pm 0.2$ μm. The flow of particles through the Y-junction is then controlled by a syringe pump (New Era Pumping Systems) with a flow rate of $0.1\,\mu\text{L min}^{-1}$.

As the chain of particles approaches the bifurcation channels an external field is applied. The magnetic field is controlled by a pair of coils aligned along the $\hat{\boldsymbol{x}}$-axis, parallel to the chain of particles in the straight channel, and a third coil situated beneath the microfluidic chip that generates the field component along the vertical $\hat{\boldsymbol{z}}$-axis. By methodically superimposing the field components along the two axes we can control the angle of the resultant field ($\vartheta \in [0, 90]°$) applied on the particle system while keeping constant the field strength to $B = 8$ mT. The currents in the coils are powered by a bipolar operational power amplifier (KEPCO BOP) and controlled by a LabVIEW program. The field strengths in each axis are linearly correlated as a function of the current, I: $B_x(\text{mT}) = 1.0601 \cdot I(\text{A}) + 0.0613$, $B_z(\text{mT}) = 5.0215 \cdot I(\text{A}) + 0.3181$.

The microfluidic chip and coils are also integrated within a custom-built optical microscope equipped with a 10 × Nikon objective, a Basler area scan camera (5–20 fps, acA640-750uc) and illuminated with a Thorlabs White mounted LED (MWWHL4) to observe the particle dynamics taking place in the Y-junction. Image capturing is done using Basler's pylon camera software.

Additional higher resolution imaging was carried out using a Nikon Eclipse Ni microscope with a 20 × Nikon objective integrated with a similar coil system. Here the coils are powered by a power amplifier (Amp18000) and an EL302RT Triple Power Supply waveform generator. The coils were calibrated with the following correlations: $B_x(mT) = 1.8837 \cdot I(A) - 0.0028$,

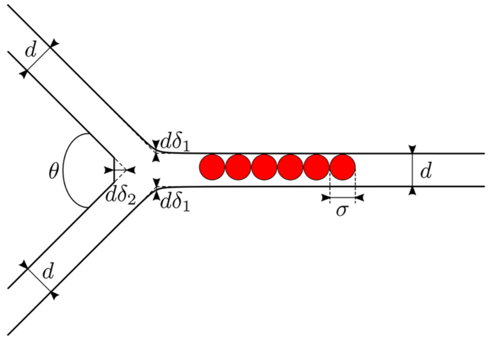

Fig. 5 | Simulation geometry of the Y-junction. Schematic illustrating the various parameters used to replicate the flat wedge of microfluidic Y-junction observed in the experimental system (see Fig. 2b).

Table 1 | Simulation parameters

Symbol	Meaning	Value & relations
m	Magnetic dipole moment	$m = \chi BV/\mu_0$
χ	Magnetic susceptibility	$\chi = 0.014$
B	Magnetic field	$B = 8$ mT
μ_0	Permeability of the medium	$\mu_0 = 4\pi \times 10^{-7}$ N/A^2
V	Volume	$V = \pi\sigma^3/6$
ϑ	Resultant field angle	$\vartheta \in [0, 90]°$
σ	Polysterene (effective) particle size	$\sigma = 18.82$ μm
$\sigma_{\rm sim}$	Particle size used in simulations	$\sigma_{\rm sim} = 0.89\sigma$
ε	Dispersion energy	$\varepsilon\sigma^3/\mu_0 m^2 = 0.54$
d	Channel width	$d = 26.1$ μm
θ	Bifurcation angle	$\theta = 90°$
$\delta_{1,2}$	Lithography imperfection parameters	$\delta_1 = 0.110$, $\delta_2 = 0.375$
ρ	Fluid density	$\rho = 10^3$ kg/m^3
ν	Kinematic viscosity	$\nu = 10^{-3}$ Pa · s
v	Input velocity	$v = 10.5$ μm/s
$x_{\rm in,out}$	Input/output boundaries	$x_{\rm in,out} = \pm 3d$
γ	Stokes friction	$\gamma = 3\pi\nu\sigma$

Value of the parameters used in numerical simulations. These parameters align with their corresponding experimental values.

$B_z(mT) = 11.156 \cdot I(A) + 0.0791$. A Basler scA640-74fc camera with a C-mount Adapter 0.45 × (Nikon) was used with Basler's pylon camera software.

Numerical simulation details

In our simulations, which are based on the integration of Eqs. (3), we consider particles interacting via a combination of hardcore (Weeks-Chandler-Anderson) and dipole-dipole interaction, explicitly

$$U_{\rm p}(\mathbf{r}_{ij}) = U_{\rm WCA}(\mathbf{r}_{ij}) + U_{dd}(\mathbf{r}_{ij}), \tag{4a}$$

$$U_{\rm WCA}(\mathbf{r}_{ij}) = \begin{cases} 4\varepsilon\left[\left(\frac{\sigma}{r_{ij}}\right)^{12} - \left(\frac{\sigma}{r_{ij}}\right)^{6}\right], & \text{if } r_{ij}<2^{1/6}\sigma, \\ 0, & \text{else.} \end{cases} \tag{4b}$$

$$U_{dd}(\mathbf{r}_{ij}) = \begin{cases} \frac{\mu_0 m^2}{4\pi r_{ij}^3}\left(1 - 3\cos^2\vartheta\right), & \text{if } r_{ij}<1.4\sigma, \\ 0, & \text{else.} \end{cases} \tag{4c}$$

Here σ is the particle diameter, μ_0 is the magnetic permeability of the medium, $m = \chi BV/\mu_0$ is the induced dipole moment, χ is the magnetic volume susceptibility, $V = \pi\sigma^3/6$ is the particle volume, and ϑ the field angle within the $(\hat{\boldsymbol{x}}, \hat{\boldsymbol{z}})$ plane.

The particle size $\sigma_{\rm sim}$ used in the simulations is chosen so that the repulsive tail of the WCA potential has a range equal to the diameter of the polystyrene particles[71], i.e.,

$$\sigma_{\rm sim} = 2^{-\frac{1}{6}}\sigma \approx 0.89\sigma. \tag{5}$$

Dispersion energy, $\varepsilon \sim \mu_0 m^2/\sigma^3$ is chosen to be of the same order as the characteristic energy of dipole-dipole interaction[72]. For the dipole-dipole interaction, we use the cut-off distance 1.4σ which corresponds to only nearest-neighbor interactions.

The interaction with channel walls is represented by the truncated Lennard-Jones potential,

$$U_{\rm w}(\mathbf{r}_i) = \begin{cases} 4\varepsilon\left[\left(\frac{\sigma}{r_{iw}}\right)^{12} - \left(\frac{\sigma}{r_{iw}}\right)^{6}\right], & \text{if } r_{iw}<2.5\sigma, \\ 0, & \text{else.} \end{cases} \tag{6}$$

Here, $r_{iw} = |\mathbf{r}_i - \mathbf{r}_{\rm virt}|$ is the distance between the particle i and the closest wall distance with $\mathbf{r}_{\rm virt} = \mathbf{r}_{\rm wall} \pm \mathbf{e}_w^{\perp}\sigma/2$, where $\mathbf{r}_{\rm wall}$ is the actual position of the wall, $\mathbf{e}_w^{\perp}$ is the unit vector perpendicular to the direction of the wall, and the sign $+$ (or $-$) is chosen depending on the wall being on upper (lower) wall. This potential approximates a hardcore interaction combined with a long-range attractive interaction, indicating that particles tend to adhere to the walls in the experiment.

We model the walls (boundaries) of the Y-junction ∂S in two dimensions using the following curves:

$$y = \pm d\left[\frac{1+x}{2}\tan\frac{\theta}{2} + \sqrt{\frac{x^2}{4}\tan^2\frac{\theta}{2} + \delta_1^2}\right],\ x_{\rm in} \le x \le x_{\rm out} \tag{7a}$$

$$y = \pm x\tan\frac{\theta}{2} \mp d\left(\frac{1}{\cos\frac{\theta}{2}} - \frac{1}{2}\right), \tag{7b}$$

$$d\left[\frac{1}{\sin\frac{\theta}{2}} - \frac{\cot\frac{\theta}{2}}{2} + \delta_2\right] \le x < x_{\rm out}, \tag{7c}$$

$$x = d\left[\frac{1}{\sin\frac{\theta}{2}} - \frac{\cot\frac{\theta}{2}}{2} + \delta_2\right],\ |y| \le d\delta_2\tan\frac{\theta}{2}. \tag{7d}$$

Here, θ is the bifurcation angle, and d is the channel width. Eq. (7a) define the outer walls of the channel, Eq. (7c) determine the inner walls that form the bifurcation point, and Eq. (7d) address the rounding of the bifurcation edge. Parameters $\delta_{1,2}$ take into account the lithography imperfection of the produced Y-junction, with $\delta_{1,2} = 0$ corresponding to the ideal Y-junction, as shown in Fig. 5. Input is given at $x = x_{\rm in} \ll d < 0$, and output is at $x = x_{\rm out} \gg d > 0$.

The incompressible Navier-Stokes equations, Eqs. 1(a, b), are solved using the the Dirichlet boundary conditions,

$$\begin{cases} \mathbf{u} = (v, 0), & x = x_{\rm in}, \\ \mathbf{u} = (0, 0), & x \in \partial S, \\ p = 0, & x = x_{\rm out}. \end{cases} \tag{8}$$

The input velocity v is chosen to match the velocities of particles within the main channel with the data illustrated in Fig. 1(d).

In the simulations, we set particle number $N = 10$. For the results of Fig. 3b, the initial configuration is taken from the experiment. In the established laminar flow regime, particles tend to choose the branching channel that corresponds to their initial position relative to the walls of the main channel. Therefore, in Fig. 4, we use an initially aligned chain of colloids with $\rho = 1$, as shown in Fig. 2a for $\vartheta = 0°$, to eliminate the effect of particle initialization on branch selection. The stationary Navier-Stokes equations (1) are solved using a finite difference scheme on quadrilateral finite element meshes, with a mesh parameter of $\Delta x = 10^{-3}d$. The equations of motion (3) are solved using the Euler-Maruyama scheme with a time step of $\Delta t = 10^{-4}$. Table 1 provides all numerical values used in our simulation.

Data availability

The experimental data and simulation for all figures in the main text of this work are provided in Supplementary Data 1. Other data that support the findings of this study are available from the corresponding author upon request.

Code availability

The simulation code that supports the plots within this paper is available from the corresponding author upon reasonable request.

Received: 31 January 2025; Accepted: 7 April 2025;
Published online: 16 April 2025

References

1. Hulme, S. E. et al. Using ratchets and sorters to fractionate motile cells of escherichia coli by length. *Lab Chip* **8**, 1888 (2008).
2. Höfling, F. & Franosch, T. Anomalous transport in the crowded world of biological cells. *Rep. Progr. Phys.* **76**, 046602 (2013).
3. Altshuler, E. et al. Flow-controlled densification and anomalous dispersion of e. coli through a constriction. *Soft Matter* **9**, 1864 (2013).
4. Burada, P. S. et al. Entropic particle transport in periodic channels. *Biosystems* **93**, 16 (2008).
5. Reichhardt, C. O. & Reichhardt, C. Clogging and transport of driven particles in asymmetric funnel arrays. *J. Phys. Condens. Matter* **30**, 244005 (2018).
6. Malgaretti, P., Oshanin, G. & Talbot, J. Special issue on transport in narrow channels. *J. Phys. Cond. Matter* **31**, 270201 (2019).
7. Dzubiella, J. & Hansen, J.-P. Electric-field-controlled water and ion permeation of a hydrophobic nanopore. *J. Chem. Phys.* **122**, 234706 (2005).
8. Yang, S., Ündar, A. & Zahn, J. D. A microfluidic device for continuous, real time blood plasma separation. *Lab Chip* **6**, 871 (2006).
9. Jäggi, R. D., Sandoz, R. & Effenhauser, C. S. Microfluidic depletion of red blood cells from whole blood in high-aspect-ratio microchannels. *Microfluid Nanofluid* **3**, 47 (2007).
10. Genovese, D. & Sprakel, J. Crystallization and intermittent dynamics in constricted microfluidic flows of dense suspensions. *Soft Matter* **7**, 3889 (2011).
11. Kreuter, C., Siems, U., Nielaba, P., Leiderer, P. & Erbe, A. Transport phenomena and dynamics of externally and self-propelled colloids in confined geometry. *Eur. Phys. J. Spec. Top.* **222**, 2923 (2013).
12. Sendekie, Z. B. & Bacchin, P. Colloidal jamming dynamics in microchannel bottlenecks. *Langmuir* **32**, 1478 (2016).
13. Zuriguel, I. et al. Silo clogging reduction by the presence of an obstacle. *Phys. Rev. Lett.* **107**, 278001 (2011).
14. Thomas, C. C. & Durian, D. J. Fraction of clogging configurations sampled by granular hopper flow. *Phys. Rev. Lett.* **114**, 178001 (2015).
15. Zeineddine, H. A dynamically optimized aircraft boarding strategy. *J. Air Transp. Manag.* **58**, 144 (2017).
16. Wittmann, J. Customer-oriented optimization of the airplane boarding process. *J. Air Transp. Manag.* **76**, 31 (2019).
17. Reynolds, C. C., Harris, M. A., Teschke, K., Cripton, P. A. & Winters, M. The impact of transportation infrastructure on bicycling injuries and crashes: a review of the literature. *Environm. Health* **8**, 1 (2009).
18. Helbing, D., Farkas, I. & Vicsek, T. Simulating dynamical features of escape panic. *Nature* **407**, 487 (2000).
19. Zuriguel, I. et al. Clogging transition of many-particle systems flowing through bottlenecks. *Sci. Rep.* **4**, 7324 (2014).
20. Kirchner, A., Nishinari, K. & Schadschneider, A. Friction effects and clogging in a cellular automaton model for pedestrian dynamics. *Phys. Rev. E* **67**, 056122 (2003).
21. Gella, D. et al. Linking bottleneck clogging with flow kinematics in granular materials: the role of silo width. *Phys. Rev. Fluids* **2**, 084304 (2017).
22. Yang, J., Pak, Y. E. & Lee, T. R. Predicting bifurcation angle effect on blood flow in the microvasculature. *Microvasc. Res.* **108**, 22 (2016).
23. Shen, Z. et al. Anomalous diffusion of deformable particles in a honeycomb network. *Phys. Rev. Lett.* **130**, 014001 (2023).
24. Jorge, C., Chardac, A., Poncet, A. & Bartolo, D. Active hydraulics laws from frustration principles. *Nat. Phys.* **20**, 303 (2024).
25. Li, J., Papadopoulos, C. & Xu, J. Growing Y-junction carbon nanotubes. *Nature* **402**, 253 (2016).
26. Garstecki, P., Fuerstman, M. J., Stone, H. A. & Whitesides, G. M. Formation of droplets and bubbles in a microfluidic t-junction-scaling and mechanism of breakup. *Lab Chip* **6**, 437 (2006).
27. Vigolo, D., Radl, S. & Stone, H. A. Unexpected trapping of particles at a t junction. *Proc. Natl. Acad. Sci. USA* **111**, 4770 (2006).
28. Ollila, S. T. T., Denniston, C. & Ala-Nissila, T. One- and two-particle dynamics in microfluidic t-junctions. *Phys. Rev. E* **87**, 050302 (2013).
29. Iyer, P., Negi, R. S., Schadschneider, A. & Gompper, G. Directed motion of cognitive active agents in a crowded three-way intersection. *Comm. Phys.* **7**, 379 (2024).
30. Wyss, H. M., Blair, D. L., Morris, J. F., Stone, H. A. & Weitz, D. A. Mechanism for clogging of microchannels. *Phys. Rev. E* **74**, 061402 (2006).
31. Dressaire, E. & Sauret, A. Clogging of microfluidic systems. *Soft matter* **13**, 37 (2017).
32. Tang, J. & Behringer, R. P. Orientation, flow, and clogging in a two-dimensional hopper: ellipses vs. disks. *Europhys. Lett.* **114**, 34002 (2016).
33. Haw, M. D. Jamming, two-fluid behavior, and “self-filtration” in concentrated particulate suspensions. *Phys. Rev. Lett.* **92**, 185506 (2004).
34. Köppl, M., Henseler, P., Erbe, A., Nielaba, P. & Leiderer, P. Layer reduction in driven 2d-colloidal systems through microchannels. *Phys. Rev. Lett.* **97**, 208302 (2006).
35. Borromeo, M., Marchesoni, F. & Ghosh, P. Communication: driven brownian transport in eccentric septate channels. *J. Chem. Phys.* **134**, 051101 (2011).
36. Martens, S., Straube, A. V., Schmid, G., Schimansky-Geier, L. & Hänggi, P. Hydrodynamically enforced entropic trapping of brownian particles. *Phys. Rev. Lett.* **110**, 010601 (2013).
37. Siems, U. & Nielaba, P. Transport and diffusion properties of interacting colloidal particles in two-dimensional microchannels with a periodic potential. *Phys. Rev. E* **91**, 022313 (2015).
38. Glanz, T., Wittkowski, R. & Löwen, H. Symmetry breaking in clogging for oppositely driven particles. *Phys. Rev. E* **94**, 052606 (2016).
39. Hidalgo, R. C., Goñi Arana, A., Hernández-Puerta, A. & Pagonabarraga, I. Flow of colloidal suspensions through small orifices. *Phys. Rev. E* **97**, 012611 (2018).
40. Ghosh, P. K. et al. Driven brownian transport through arrays of symmetric obstacles. *Phys. Rev. E* **85**, 011101 (2012).
41. Gerloff, S., Vezirov, T. A. & Klapp, S. H. L. Shear-induced laning transition in a confined colloidal film. *Phys. Rev. E* **95**, 062605 (2017).
42. Zimmermann, U. et al. Negative resistance for colloids driven over two barriers in a microchannel. *Soft Matter* **17**, 516 (2021).
43. Siems, U. et al. Non-monotonic crossover from single-file to regular diffusion in micro-channels. *Sci. Rep.* **2**, 59 (2012).

44. Heinze, B., Siems, U. & Nielaba, P. Segregation of oppositely driven colloidal particles in hard-walled channels: a finite-size study. *Phys. Rev. E* **92**, 012323 (2015).
45. Foulaadvand, M. E. & Aghaee, B. Driven binary colloidal mixture in a 2d narrow channel with hard walls. *Eur. Phys. J. E* **39**, 37 (2016).
46. Sochi, T. Fluid flow at branching junctions. *Inter. J. Fluid Mech. Res.* **42**, 59 (2015).
47. Zhang, J., Grzybowski, B. A. & Granick, S. Janus particle synthesis, assembly, and application. *Langmuir* **33**, 6964 (2017).
48. Xiao, Z., Nsamela, A., Garlan, B. & Simmchen, J. A platform for stop-flow gradient generation to investigate chemotaxis. *Angew. Chem. Int. Ed.* **61**, e202117768 (2022).
49. Grafton, M. et al. Design of a multi-stage microfluidics system for high-speed flow cytometry and closed system cell sorting for cytomics, in *Imaging, Manipulation, and Analysis of Biomolecules, Cells, and Tissues VI*, Vol. 6859, (eds Farkas, D. L., Nicolau, D. V., and Leif, R. C.) International Society for Optics and Photonics (SPIE, 2008).
50. Taloni, A. & Marchesoni, F. Single-file diffusion on a periodic substrate. *Phys. Rev. Lett.* **96**, 020601 (2006).
51. Barkai, E. & Silbey, R. Theory of single file diffusion in a force field. *Phys. Rev. Lett.* **102**, 050602 (2009).
52. Illien, P., Bénichou, O., Mejía-Monasterio, C., Oshanin, G. & Voituriez, R. Active transport in dense diffusive single-file systems. *Phys. Rev. Lett.* **111**, 038102 (2013).
53. Dolai, P. et al. Universal scaling in active single-file dynamics. *Soft Matter* **16**, 7077 (2020).
54. Cereceda-López, E. et al. Hydrodynamic interactions can induce jamming in flow-driven systems. *Phys. Rev. Lett.* **127**, 214501 (2021).
55. Isa, L., Besseling, R., Morozov, A. N. & Poon, W. C. K. Velocity oscillations in microfluidic flows of concentrated colloidal suspensions. *Phys. Rev. Lett.* **102**, 058302 (2009).
56. Campbell, A. I. & Haw, M. D. Jamming and unjamming of concentrated colloidal dispersions in channel flows. *Soft Matter* **6**, 4688 (2010).
57. Kanehl, P. & Stark, H. Self-organized velocity pulses of dense colloidal suspensions in microchannel flow. *Phys. Rev. Lett.* **119**, 018002 (2017).
58. Sarkar, T., Chaudhuri, P. & Sain, A. Poiseuille flow of soft polycrystals in 2d rough channels. *Phys. Rev. Lett.* **124**, 158003 (2020).
59. Yang, R. & Wang, W. A numerical and experimental study on gap compensation and wavelength selection in uv-lithography of ultra-high aspect ratio su-8 microstructures. *Sensors Actuators B Chem.* **110**, 279 (2005).
60. Simmchen, E.J., Uspal, W. & Wang, W. *Active Colloids: From Fundamentals to Frontiers* (Royal Society of Chemistry, 2024).
61. Tierno, P., Schreiber, S., Zimmermann, W. & Fischer, T. M. Shape discrimination with hexapole-dipole interactions in magic angle spinning colloidal magnetic resonance. *J. Am. Chem. Soc.* **131**, 5366 (2009).
62. Truskey, G. A., Yuan, F. & Katz, D. F. *Transport Phenomena in Biological System* (Pearson/Prentice Hall, Upper Saddle River, 2004).
63. Dupire, J., Puech, P.-H., Helfer, E. & Viallat, A. Mechanical adaptation of monocytes in model lung capillary networks. *Proc. Natl. Acad. Sci. USA* **117**, 14798 (2020).
64. DiLuzio, W. R. et al. Escherichia coli swim on the right-hand side. *Nature* **435**, 1271 (2005).
65. Tusona, H. H. & Weibel, D. B. Bacteria-surface interactions. *Soft Matter* **9**, 4368 (2013).
66. Yethiraj, A. & van Blaaderen, A. A colloidal model system with an interaction tunable from hard sphere to soft and dipolar. *Nature* **421**, 513 (2003).
67. Leunissen, M. E. et al. Ionic colloidal crystals of oppositely charged particles. *Nature* **437**, 235 (2005).
68. Lekkerkerker, H. N. W., Tuinier, R. & Vis, M. *Colloids and the Depletion Interaction* (Springer, 2011).
69. Feng, L., Laderman, B., Sacanna, S. & Chaikin, P. Re-entrant solidification in polymer-colloid mixtures as a consequence of competing entropic and enthalpic attractions. *Nature Mat.* **14**, 61 (2015).
70. Junot, G., De Corato, M. & Tierno, P. Large scale zigzag pattern emerging from circulating active shakers. *Phys. Rev. Lett.* **131**, 068301 (2023).
71. Barker, J. A. & Henderson, D. What is "liquid"? understanding the states of matter. *Rev. Mod. Phys.* **48**, 587 (1976).
72. Kaiser, A., Popowa, K. & Löwen, H. Active dipole clusters: from helical motion to fission. *Phys. Rev. E* **92**, 012301 (2015).

Acknowledgements

This project has received funding from the European Research Council (ERC) under the European Union's Horizon 2020 research and innovation program (grant agreement no. 811234). P.T. acknowledges support from the Ministerio de Ciencia e Innovación (Project No. PID2022-137713NB-C22), the Agència de Gestió d'Ajuts Universitaris i de Recerca (Project No. 2021 SGR 00450) and the Generalitat de Catalunya under Program "ICREA Acadèmia". A.A. and H.L. acknowledge funding from the DFG within project LO418/29-1.

Author contributions

M.T. and C.R.G. performed the experiments. F.J.S. and A.A. run the numerical simulations. P.T. and H.L. supervised the work. All authors discussed the results and commented on the manuscript at all stages.

Competing interests

The authors declare no competing interests.

Additional information

Supplementary information The online version contains supplementary material available at https://doi.org/10.1038/s42005-025-02094-1.

Correspondence and requests for materials should be addressed to Pietro Tierno.

Peer review information *Communications Physics* thanks the anonymous reviewers for their contribution to the peer review of this work. A peer review file is available.